U.S. Department of Commerce
National Oceanic and Atmospheric Administration
National Weather Service
National Centers for Environmental Prediction
5830 University Research Court
College Park, MD 20740-3818

Office Note 504

https://doi.org/10.25923/0sv0-4916

Single Column Model Evaluations of Mixing Length Formulations and Constraints for the sa-TKE-EDMF Scheme

Edward Strobach[1,2]

[1]I.M. Systems Group, Inc., Rockville, Maryland; [2]NOAA/NWS/NCEP Environmental Modeling Center, College Park, Maryland

March, 2021

E-mail: Edward.Strobach@noaa.gov

Abstract

Parameterizing boundary layer turbulence is a critical component of numerical weather prediction and the representation of turbulent mixing of momentum, heat, and other tracers. The components that make up a boundary layer scheme can vary considerably, with each scheme having a combination of processes that are physically represented along with tuning parameters that optimize performance. Isolating a component of a PBL scheme to examine its impact is essential for understanding the evolution of boundary layer profiles and their impact on the mean structure. In this study we conduct three experiments with the sa-TKE-EDMF scheme: 1) releasing the upper limit constraints placed on mixing lengths, 2) incrementally adjusting the tuning coefficient related to wind shear in BouLac mixing length formulation, 3) replacing the current mixing length formulations with those used in the MYNN scheme. A diagnostic approach is adopted to characterize the bulk representation of turbulence within the residual layer and boundary layer in order to understand the importance of different terms in the TKE budget as well as to assess how the balance of terms changes between mixing length formulations. Although our study does not seek to determine the best formulation, it was found that strong imbalances led to considerably different profile structures, both in terms of the resolved and subgrid fields, that led to undesirable results. Experiments where this balance was preserved shows a minor impact on the mean structure regardless of the turbulence generated. Overall, it was found that changes to mixing length formulations and/or constraints had stronger impacts during the day while remaining partially insensitive during the evening.

1. Introduction

A central component of numerical weather prediction is the physical representation of subgrid-scale processes that influence the mean dynamic/thermodynamic structure. Parameterizing processes such as convection, boundary layer turbulence, cloud microphysics, and gravity wave drag are therefore essential to achieve accurate forecasts across a variety of time and spatial scales. Extensive research and development of parameterizations has led to copious representations of the same subgrid process, all of which are intended to improve the prediction and representation of different weather regimes (Mellor and Yamada 1974; Lin et. al. 1983; Randall and Pan 1993; Janic 2001; Morrison and Gettlemen 2008; Thompson et. al. 2008; Grell and Freitas 2014; Han et. al. 2017; Aligo et. al. 2018; Han and Bretherton 2019; amongst others). Since the schemes developed are tested alongside parameterizations of other subgrid-scale processes, then it is more than likely that they have been tuned together in a single package to maximize forecast performance (Voudouri et. al. 2017; Cowan et. al. 2019). This has resulted in schemes becoming semi-physical and rigid in the sense that improved performance is done by 'expert tuning' based on subjective analysis rather than observational evidence (Duan et. al. 2006; Voudouri et. al. 2017). Not surprisingly, running forecast models using a suite of schemes is highly recommended based on the extended history schemes in each suite have with one another, particularly as it relates to their co-evolution. In other words, replacing a parameterization with one that is more robust in terms of its representation of physical processes may still produce a worse forecast because it has not been tuned or adjusted to work well with other schemes in that suite.

Despite being presented with a lack of 'commutability' when pairing various parameterizations, there are ways one can approach this problem. The first is understanding that the parameterization of each process has the same goal in mind and therefore must share some basic assumptions regardless of scheme layout. In the case of parameterizing boundary layer turbulence, most schemes assume horizontally homogeneous turbulence and apply a downgradient approach to represent local mixing (Abdella and McFarlane 1997; Baklanov et. al. 2011). Non-local components are done either by adopting a mass flux approach (Pleim 2007; Siebesma et. al. 2007), making use of counter-gradient correction terms (Troen and Mahrt 1986; Noh et. al. 2003), or predicting higher order moments (Grossman 1996; Mishra and Girimaji, 2017). A divergence between PBL schemes tends to lie in the representation of how the mixing lengths, stability functions, and entrainment are represented (Mellor and Yamada 1974; Mellor and Yamada 1982; Bougeault and Lacarrere 1989; Nakanish 2001; Nakanishi and Niino 2004; Teixeira and Cheinet 2004; Siebesma et. al. 2007; Tian and Kuang 2016); how cloud-topped PBLs are treated (Lock et. al. 2000; Siebesma et. al. 2007); what variables are being prognosed (Janic 2001; Nakanishi and Niino 2004; Han and Bretherton 2019); the order by which the computations are being made in the parameterization; and the tuning history. Similar examples are undoubtedly found for other physical parameterizations representing different physical processes.

The second approach is to find ways to isolate areas that lead to poor performance. From an operational perspective, it is well understood for short-to-medium range forecasts that model solutions using different physics can diverge significantly for precipitation forecasts, storm track and initiation, the representation of cloud cover, or the diurnal structure (Chakraborty 2010; Cuo et. al. 2011; Zhang et. al. 2013; Lamberson et. al. 2016). Although potentially cumbersome, it may prove instructive to focus on a particular scheme tied to an issue and run iterative experiments that either test different assumptions or apply different tuning coefficients in order to understand the sensitivity of the result and its impact on a particular problem. This can be done

by running a full forecast, through single column model (SCM) experiments, with a Large Eddy Simulation (LES), or a combination thereof.

Following this line of reasoning, we aim to focus our efforts on the sa-TKE-EDMF PBL scheme that is slated to replace the operational GFS PBL scheme in the next version of the Finite Volume (FV3) Cubed Sphere modeling system. Instead of interrogating the sa-TKE-EDMF scheme to its entirety, we focus strictly on examining the sensitivity of the mixing length component since it has an integral role in parameterizing both the diffusivity coefficients and dissipation (Han and Bretherton 2019; Olson et. al. 2019). Several sensitivity experiments are run to examine the diurnal structure in a SCM setting by 1) comparing the diurnal structure when removing constraints to the size of the mixing length – currently set to 300-m – 2) including a wind shear dependent mixing length formulation to the BouLac (Bougeault and Lacarrere) mixing length with an adjustable coefficient, and 3) testing an alternative representation of both the surface layer and turbulent/buoyancy length scales adopted from the Mellor-Yamada-Nakanishi-Niino (MYNN) scheme.

The SCM case chosen for this study is based on the GEMWEX (Global Energy and Water Exchange) Atmospheric Boundary-Layer Study (GABLS3) since it features a case that is not complicated by clouds and thus offers an opportunity to study an arguably simple regime (Bosveld et al. 2014). Particular attention will be paid to the transition periods, and the differences in the vertical structure and how it relates to adjustments to different mixing length considerations. These results are not meant to offer preferred formulations or tuning coefficients, but rather to shine light on the sensitivity of our choices and why we make them. It's understood that this case alone does not represent a full picture, but rather offers a simple case that can be used to examine these sensitivities. Our goal is therefore to understand how the sa-TKE-EDMF scheme responds to the proposed experiments for evaluating mixing lengths.

The remainder of the paper is as follows. First, is a discussion of the case set-up and experimental design. Second, we discuss the sa-TKE-EDMF scheme and the mixing length formulations used. Third, we present the results of all three experiments and evaluate the bulk energetics and the mean structure spanning a diurnal cycle of the GABLS3 case. Fourth, is further discussion of results and how findings from section 4 translates to differences in the vertical structure of turbulent and mean fields. Lastly are the conclusions drawn from this study.

2. Case Set-up

a. Single Column-Model

In this study we conduct our analyses using output generated from the single column model (SCM). The SCM is an integral part of the common-community physics package (CCPP) available for testing, research, and development. It is maintained by both developers at the developmental testbed center (DTC) as well as researchers external to DTC. Several cases are available to offer a diverse selection of weather regime types. In this study we focus on the third GEMWEX (Global Energy and Water Exchange) Atmospheric Boundary-Layer Study (GABLS3).

Unlike 3-D global and mesoscale model simulations, the SCM can be run with one or more vertical columns, all of which depend on a set of initial conditions, large-scale and lateral forcing, and surface boundary conditions to integrate forward in time. The SCM may be stationary or transiting depending on whether the observational data used to force the SCM is on a stationary or moving platform. For GABLS3, the SCM is maintained in a stationary frame of reference and is run as a single column occupying an area of 1.45e8 m2. The output

consists of 64 vertical levels with a model top of 0.4-mb. The model time step and output frequency is identically set to 600-s with calls to radiation occurring every hour. The time integration method is configured using a forward Eulerian time-stepping scheme. For thermodynamic and momentum forcing we run by advecting horizontal tendencies of temperature, moisture, and momentum while prescribing vertical motion. Both geostrophic components are set to 2m/s above 800-mb. In order to match the conditions of the Cabauw site during the allotted time period for this study, a roughness length of 15.0 cm was chosen with MODIS derived albedos incorporated to reflect the surface as observed during the GABLS3 time period.

b. GABLS3

The decision to choose GABLS3 for this study was largely influenced by its simplicity; namely it features a single diurnal cycle free from precipitation and cloud contamination. The specific case analyzed is identical to that presented by Bosveld et al. (2014), which coincides with the development of a strong nocturnal Low-Level Jet (LLJ). Although this case only represents a single 24-hour period extending from July 1, 2006 to July 2, 2006, we believe that the night-to-day transition in the latter part of the simulation may offer some key insight when examining the treatment of mixing length formulations and the impact it has on the stable-to-convective boundary layer transition. Since we are testing mixing length formulations for a particular scheme, it should be cautioned that degraded performance may not be the result of the mixing length options chosen, but rather how the mixing length formulation interacts with other assumptions/components within the the parameterization being tested. Therefore, it should be understood that some studies showing positive results for a particular scheme may be subject to this interplay.

The site where GABLS3 was conducted is located in the western Netherlands, and is approximately 50-km from the North Sea (Bosveld et al. 2014). The change in elevation is small, consisting mostly of grassland. The site hosts a tower with other nearby observations that are integrated into the validation part of this study. The subtle variation in topography is yet another reason for choosing this case since it is not complicated further by complex terrain. Readers can refer to Bosveld et. al. (2014) for additional details about the Cabuaw site.

c. Observations

Two sets of observations are used to compare with the model output in this study: the Cabauw tower and soundings that were launched twice daily. The tower, which is geographically co-located with the SCM, reports 10-minute averaged values of turbulent fluxes of momentum, heat, and moisture as well as temperature and wind data. The measurements on the tower consist of an array of sonic anemometers at heights of z=10, 20,40, 80,140, and 200-m (Bosveld et. al. 2014). The soundings are launched from the De Bilt station located about 25-km north-east of Cabauw. We combine these observations in the discussion part of the paper when examining individual profiles.

d. Experimental Design and Physics

Three experiments are run in this study. The first removes the upper limit constraint of 300-m for the mixing length scales on the surface layer length scale, asymptotic length scale, or both, and compares that with the control case (i.e. original settings – CTRL). The second set of experiments compares the control with the application of a modified BouLac (Bougeault

and Lacarrere) mixing length with different shear coefficients (0.25, 0.5, 0.75, and 1.). The third compares CTRL with an experiment that replaces the current mixing length formulations with MYNN mixing length formulations. All remaining physics options are identically set, with the double moment Thompson microphysics (Thompson et. al 2008), SA-MF shallow and deep convection (Han et. al. 2016), and gravity wave drag parameterizations used in the suite configuration. Calls to radiation use RRMTG while Noah is used to represent the land surface. We also use the GFS surface layer scheme since it has been extensively tested with the sa-TKE-EDMF PBL parameterization.

3. The sa-TKE-EDMF Scheme and Formulation of Mixing Lengths

a. Prognosing TKE

The sa-TKE-EDMF scheme is a scale aware eddy diffusivity mass flux PBL parameterization that prognoses TKE. The governing equation used to update TKE (i.e. $\bar{e}$) every time step in equation (1) consists of the buoyancy (BP) and shear production (SP) terms, TKE and mass transport terms (T), and dissipation (D) on the right hand side, respectively.

$$\frac{\partial \bar{e}}{\partial t} = \underbrace{\frac{g}{T_{v0}}\overline{w'\theta_v'}}_{BP} - \underbrace{\left(\overline{w'u'}\frac{\partial U}{\partial z} + \overline{w'v'}\frac{\partial V}{\partial z}\right)}_{SP} - \underbrace{\frac{\partial}{\partial z}\left(\overline{w'e'} + \frac{1}{\rho}\overline{w'p'}\right)}_{T} - \underbrace{\varepsilon}_{D} \tag{1}$$

The form of equation 1 is simplified by the assumption that turbulence is horizontally homogeneous. Although this assumption is widely considered adequate for numerical modeling, it may breakdown for baroclinic type flows, coastal flows, or flows over complex terrain under certain horizontal resolutions (Baklanov et. al. 2011; Munoz et al. 2016). For the eddy diffusivity (ED) component of the parameterization, the flux terms on the right hand side of equation (1) are calculated using a down-gradient approach shown by equation (2).

$$\overline{w'\phi'} = -K_\phi \frac{\partial \Phi}{\partial z} \tag{2}$$

where ϕ represents any field susceptible to mixing such as temperature, moisture, or wind; and the K_ϕ is the mixing coefficient for the arbitrary quantity, ϕ. In the sa-TKE-EDMF scheme, the mixing coefficient is calculated for momentum, heat, moisture, and TKE, with the coefficient assumed equal for the last three variables. The relationship between the eddy diffusivity and viscosity is defined by the Prandtl Number in equation (3), which is a useful metric for understanding the relative exchange of heat and momentum.

$$Pr = \frac{K_m}{K_h} \tag{3}$$

The Prandtl Number is further parameterized using formulations from Han et. al. (2019).

Dissipation is parameterized by TKE prior to stepping forward in time and a mixing length scale shown by equation 4, where

$$\varepsilon = C\frac{\bar{e}^{\frac{3}{2}}}{L_\varepsilon} \tag{4}$$

L_ε represents a blended mixing scale related to the Boulac formulation (equation 11b) and C represents a constant currently set to 1. The mass flux (MF) component of the scheme follows Seibesma et al. (2007), which determines a mass flux updraft/downdraft velocity component (M) as well as a parcel calculation of the variable being parameterized (Φ_u or Φ_d). Together, along with an LES derived entrainment profile in their paper, the full flux parameterization of any field can be expressed by equation (5) as

$$\overline{w'\phi'} = -K_\phi \frac{\partial \Phi}{\partial z} + M_{\phi,u}(\Phi_u - \Phi) - M_{\phi,d}(\Phi_d - \Phi) \quad (5)$$

where the first term on the right hand side represents the ED component while the last two terms represent the mass flux terms for both convective conditions and cloud-topped PBLs, respectively.

Out of the above formulations, the only quantities that depend on the mixing length formulation are the mixing coefficients (K_ϕ) and turbulent dissipation (ε), and as such the dependency on the mixing length formulations partially lies in the ED portion of the sa-TKE-EDMF scheme. Since the mass flux components dominate during the day and cloudy conditions, then the ED portion of the parameterization is likely to have a secondary effect when the MF component is activated. However, any adjustments to ED, whether day or night, may have ramifications during transitional periods as well as when the PBL becomes MF-dominated. Lastly, since GABLS3 features a cloudless time period, equation (5) can be simplified to a two term expression with the last term assumed negligible.

b. Formulation of Mixing lengths

There are many approaches to assigning and blending mixing lengths for the surface layer and boundary layer. The surface layer length scale (l_s) – first described by Prandtl in 1932 – has been modified significantly over the years to account for different stability regimes (Blackadar 1962; Lenderink and Holtstag 2004; Nakanishi and Niino 2004; Sun 2011). Many PBL schemes have adopted the approach by Nakanish (2001) which is conditioned based on a non-dimensional stability parameter ($\zeta = z/L$). The different representations are consistent with other studies except for the coefficients used (Olson et. al. 2019). Equation (6) shows a general form of the surface layer lengths scales with tuning coefficients represented by a_1, a_2, a_3, b_1, and b_2.

$$l_s = \begin{cases} \kappa z(1 - a_1\zeta)^{b_1}, & \zeta < 0 \\ \kappa z(1 + a_2\zeta)^{b_2}, & 0 \le \zeta < 1 \\ a_3\kappa z, & \zeta \ge 1 \end{cases} \quad (6)$$

In the above expression, κ represents the Von Karman constant which is set to 0.4. Table 1 lists the coefficients used in the sa-TKE-EDMF as well as for two versions of the MYNN scheme. The two representations for MYNN are based on extensive tests conducted by Olson et al. (2019), with the coefficients from the second of the two versions currently set. We adopt these settings in order to examine how running with MYNN length scales differ from the control case.

	sa-TKE-EDMF	MYNN-v1	MYNN-v2
a_1	100	100	20
a_2	2.7	2.7	2.3
a_3	1/3.7	n/a	n/a
a_4	n/a	0.23	0.23
a_5	n/a	0.4	0.4
b_1	0.2	0.2	0.2
b_2	-1	-1	-1

Table 1: Tuning coefficients used in current versions of the sa-TKE-EDMF and MYNN PBL schemes.

As with the length scales for the surface layer, there exists different representations of length scales for the bulk of the boundary layer. The sa-TKE-EDMF scheme uses the BouLac formulation given by equation (7), which finds the upper/lower bounds of the two integrals l_{up} and l_{down} by determining the depth over which the integrated buoyancy is equivalent to the TKE at the initial level, z, of an ascending or descending parcel (Bougeault and Lacarrere 1989).

$$\int_{z}^{z+l_{up}} \left[\beta\left(\theta_v(z') - \theta_v(z)\right) + c_0\sqrt{\bar{e}}S(z')\right]dz' = \bar{e}(z)$$
$$\int_{z-l_{down}}^{z} \left[\beta\left(\theta_v(z) - \theta_v(z')\right) + c_0\sqrt{\bar{e}}S(z')\right]dz' = \bar{e}(z) \quad (7)$$

Once the equality has been satisfied, a length scale for both an ascending and descending parcel is determined. In addition to the buoyancy calculation, which uses the virtual potential temperature (θ_v) and buoyancy parameter (β), is a second term added to (7) to account for wind shear (S) based on dimensional arguments in Rodier et. al. (2017). The effect of including a wind shear term is to account for stratification of the flow by wind in addition to temperature. A tuning coefficient in front of the wind shear term, c_0 (SC in figures), is set to 0.5 in Rodier et. al. (2017); but, based on recent tests conducted with equation (7) at the Environmental Modeling Center (EMC), it is currently set to 0.2. Although not implemented yet into operations, the modified BouLac expression is slated to replace the original formulation in the next version release of the FV3 model. In this study we will test a range of c_0 (0, 0.25, 0.5, 0.75, and 1) in order to examine the sensitivity of this parameter to the profile structure. The effect of this modification will be of particular interest since the GABLS3 case used features a LLJ.

In order to fully test the length scales used in MYNN, we also carry over the turbulent (l_t) and buoyancy length scale (l_b) formulation. The turbulent length scale is based on the original work of Mellor and Yamada (1974) and is shown by equation (8)

$$l_t = a_4 \frac{\int_0^{h+\Delta z} \sqrt{2\bar{e}}z\,dz}{\int_0^{h+\Delta z} \sqrt{2\bar{e}}\,dz} \quad (8)$$

This simple formulation is modified to limit the upper bound of the integral to the height of the boundary layer (h) plus a transitional layer (i.e. $\Delta z = 0.3h$) as is done in Olson et al. (2019). The idea behind this length scale is to attempt to characterize the depth over which the bulk of the turbulence is being generated. The coefficient preceding the integral is a tuning parameter that is currently set to 0.23 in the MYNN scheme, which is also used in our analysis.

The buoyancy mixing length adds for a third length scale in the MYNN scheme. The two term expression shown in equation (9) consists of the original formulation dependent upon thermal

$$l_b = \frac{a_5\sqrt{2\bar{e}}}{N}\left(1 + \frac{a_3}{a_2}\left(\frac{q_c}{l_t N}\right)^{\frac{1}{2}}\right) \quad (9)$$

stratification and a buoyancy enhancement term (BET), where N is the Brunt-Vaisala frequency, q_c a turbulent velocity scale, and a_5 is tuning coefficient (refer to Table 1). Arguably it is the second term of this equation that may lead to a possible degradation since the surface flux term in $q_c (= \left[\frac{g}{\theta_0}\overline{w'\theta_v'}g l_t\right]^{1/3})$ is calculated differently between the schemes. Moreover, the buoyancy parameter in the MYNN scheme is over-simplified in that it uses a constant reference value of

300-K while the buoyancy parameter in the sa-TKE-EDMF changes with time. The latest version of the MYNN scheme blends equation (9) with BouLac (without the shear term included) by placing more weight on the former within the PBL and more weight for the latter in the free atmosphere. The blending scheme used to achieve this is given by equation (10).

$$\left.\begin{aligned} L_b &= l_b(1-w) + l_{BL}w \\ w &= 0.5\tanh\left(\frac{h+\Delta z}{0.5\,\Delta z}\right) + 0.5 \end{aligned}\right\} \quad (10)$$

The weighting, w, is to ensure a gradual transition of l_b to l_{BL} across the entrainment layer and into the free atmosphere (Olsen et al. 2019).

To maintain consistency with the MYNN mixing length formulation, we also adopt use of their blending technique for the master length scale. In the sa-TKE-EDMF scheme, two separate blends are used: one for the mixing coefficients, K, and another for dissipation. The blending approach for K is based on the harmonic average of the surface layer length scale and the minimum length scale between the updraft/downdraft calculations of BouLac (equation 11a) , while the approach for dissipation is through the square root of the product of the updraft and downdraft calculations (equation 11b).

$$\left.\begin{aligned} L_K &= \left(\frac{1}{l_s} + \frac{1}{\min(l_{down}, l_{up})}\right)^{-1} \\ L_\varepsilon &= \sqrt{l_{down} l_{up}} \end{aligned}\right\} \quad \begin{aligned} &(11a) \\ &(11b) \end{aligned}$$

In the MYNN scheme, the blending approach shown in equation 12 is simply the harmonic average of equations (6), (8), and (10), which, unlike the sa-TKE-EDMF scheme, is applied to both the mixing coefficient and dissipation. For this reason, we adopt a single blend when testing the MYNN mixing lengths.

$$L_\varepsilon = L_k = \left(\frac{1}{l_s} + \frac{1}{l_t} + \frac{1}{L_b}\right)^{-1} \quad (12)$$

Another important distinction between the schemes is the calculation of K. In MYNN, the stability functions are calculated separately for heat and momentum using forms from (Nakanishi and Niino 2009). Different representations of the stability functions are used when running different closure options for MYNN. In sa-TKE-EDMF, however, the mixing coefficients are calculated, in part, by a linearly decaying exchange profile across the boundary layer for heat and momentum that is on the order of the Von Karman constant. Both forms for K are shown for completeness in equation 13,

$$\left.\begin{aligned} K_\phi &= c_\phi L_k \sqrt{\bar{e}} \\ K_\phi &= S_\phi L_k \sqrt{2\bar{e}} \end{aligned}\right\} \quad \begin{aligned} &(13a) \\ &(13b) \end{aligned}$$

where 13a applies to sa-TKE-EDMF and 13b applies to MYNN. In equation 13a, the exchange coefficient is represented by c_ϕ while the stability function in equation 13b is represented by S_ϕ.

4. Results

In this section we present results from all three experiments by examining the bulk turbulence characteristics using an approach outlined in Appendix A, and by examining the difference in the mean structure w.r.t. to time. Figure 1a-d shows the potential temperature, specific humidity, wind speed, and TKE for the control case (CTRL), each with PBL height overlaid in red. The potential temperature field features a well-defined stable layer starting at forecast hour 7 before being mixed out by daytime convection that starts around forecast hour 18. The specific humidity in Fig. 1b increases as the stable boundary layer sets up, and maximizes during the morning transition before being transported and mixed to higher heights. The relatively strong LLJ is depicted by Fig. 1c, with the LLJ maximum coincident with the PBL height. A transition to convective conditions erodes the LLJ and replaces the wind profile with light and uniform conditions. Figure 1d depicts the largest amount of TKE occurring during the day, which maximizes at the close of the morning-transition. Smaller amounts of turbulence produced in the evening is a result of mechanical shear by the LLJ both below and above the LLJ maximum. Where appropriate, we compare Fig. 1 with differences in the mean structure (i.e. experiment – CTRL).

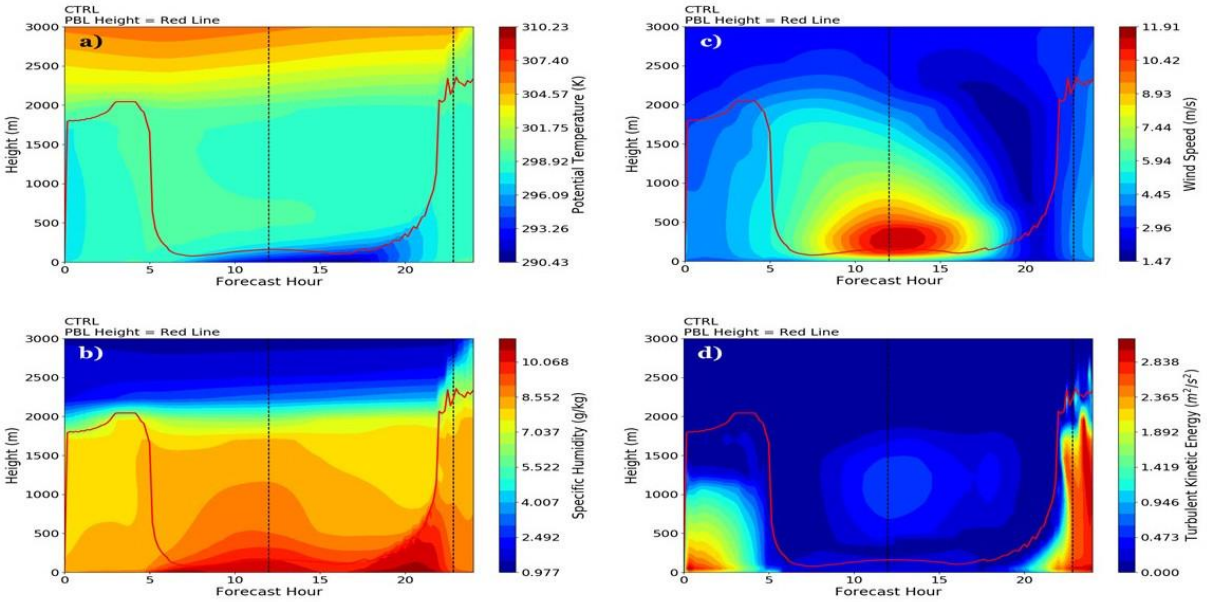

Figure 1: Time-height cross-sections of a) potential temperature, b) specific humidity, c) wind speed, and d) TKE for the CTRL run. PBL height is overlaid in red with vertical dashed lines denoting times chosen for analysis of individual profiles in the discussion section.

a. Removing mixing length constraints.

In the current version of sa-TKE-EDMF there are constraints placed on both the surface layer length scale and the asymptotic length scale, with a lower and upper bound of 10-m and 300-m, respectively. The upper limit is to ensure that the length scales do not increase to unrealistically high values. We run four experiments to examine the impact of releasing the upper bound placed on the mixing lengths: 1) releasing the surface layer constraint (ALC), 2) releasing the asymptotic length scale constraint (SLC), 3) releasing constraints on both length scales (NC), and a control that retains the constraints (CTRL). Finally, it should be noted that we only focus our analysis on the day-time boundary layer and the residual layer since asymptotic and surface layer length scales never exceed 300-m in the stable boundary layer.

We begin by showing the bulk characteristics for the entire simulation integrated over the entire PBL using equation A2. The terms included are the vertically integrated forms of equation 1, but in parameterized form; the integrated TKE tendency; and the TKE flux at the top of the PBL. Figure 2a-b compares CTRL with NC, while the other two cases are examined more closely when assessing the profile structure in the discussion section. In both situations, the buoyancy and dissipation during the day dwarfs all other terms, with dissipation largely cancelling out buoyancy production. Despite buoyancy having comparable magnitudes between CTRL and NC toward the end of the simulation, the decrease in magnitude of dissipation in Fig. 2b relative to Fig. 2a supports a net increase in the integrated TKE tendency in NC that is not shown in CTRL. Since releasing the constraint on the mixing length leads to its increase (in this case 3-fold – not shown), then the denominator in equation 4 increases. If the increase in TKE is not enough to offset the increase in the dissipation length scale in equation 11b, then the dissipation will ultimately decrease as is apparent in Fig. 2b. The other terms during the day are small, with transport closely following the behavior of the integrated TKE tendency.

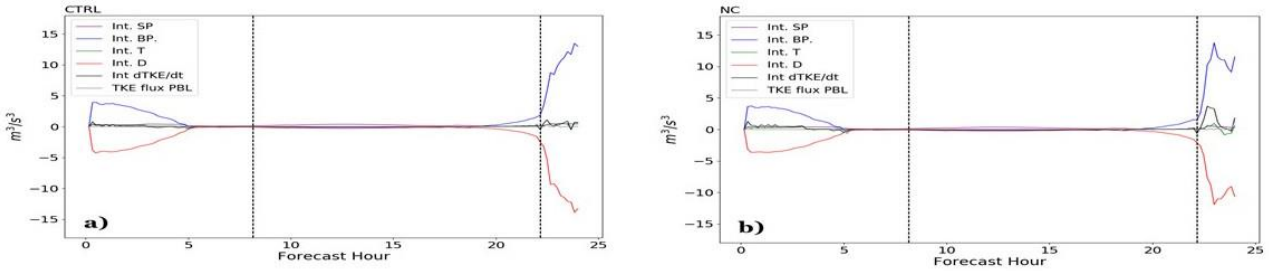

Figure 2: Vertically Integrated budget for a) CTRL and b) No Constraint (NC). The vertical dashed lines denote a zoomed in time period for stable boundary layer and the residual layer.

To isolate the nocturnal structure dwarfed by convective conditions, we zoom in on the behavior between forecast hour 8 and forecast hour 22 (between black dashed lines in Fig. 2). We only examine the residual layer in this case since releasing the mixing length constraints has no impact on the evolution of the stable boundary layer. Nevertheless, for completeness, we do include the integrated budget terms of CTRL for the stable boundary layer in Fig. 3a, which will be used in comparisons when examining other experiments. Figure 3b-c shows a subsequent ramp up in shear production and dissipation for CTRL and NC, respectively. For NC, both the magnitude of shear/buoyancy production and dissipation is larger than CTRL. The combined production in NC leads to relatively smaller decreases in the integrated TKE tendency before forecast hour 12 by offsetting dissipation. After forecast hour 12, however, the buoyancy production gradually becomes a buoyancy destruction term while shear production converges to zero by forecast hour 22. Although production increases for NC, the TKE tendency shows no detectable difference between CTRL between forecast hour 12 and 22 since dissipation increases in near proportion to the production terms. Other differences prior to the morning transition, albeit small, is a temporary increase in TKE flux across the top of the residual layer for NC prior to winds reaching maximum strength. As all terms except buoyancy converge to zero during the day-to-night transition in the residual layer, the integrated TKE tendency conforms to the buoyancy destruction term as the stratified under-layer of the stable PBL gets lifted up and overtaken by the developing convective PBL. This is evident in both CTRL and NC.

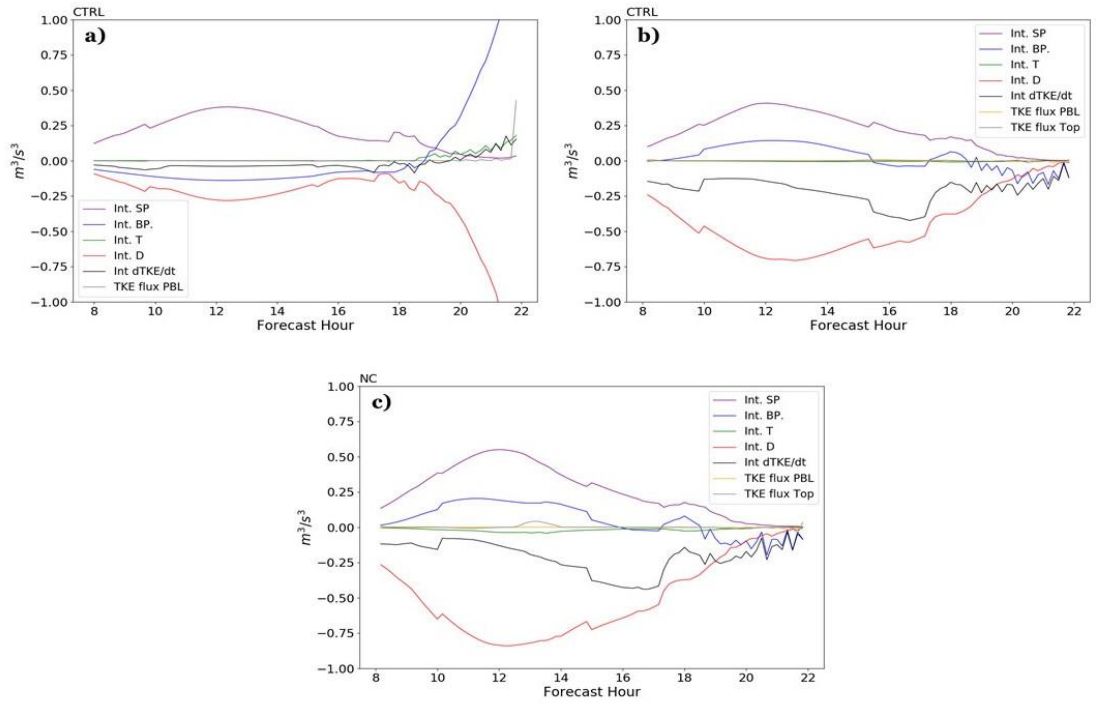

Figure 3: Vertically integrated budget for a) CTRL –stable PBL, b) CTRL – residual layer, and c) No constraint (NC) – residual layer.

The impact of removing the mixing length constraint on the mean structure is demonstrated by Fig 4a-d. The evening hours show a slightly drier and negligibly warmer PBL. The winds overall are weaker, but only by 1 m/s. Further aloft into the residual layer are gradual increases in wind speed and moisture. These features coincide with a more turbulent residual layer for NC shown in Fig. 4c. As the forecast enters the morning transition, differences in heat and moisture with alternating sign in Fig. 4a-b become apparent between NC and CTRL. These differences can be traced back to the initial amount of moisture above the residual layer that then gets mixed down during the onset of convection. The transition toward a moisture sink in the upper portion of the convective PBL for NC relative to CTRL around forecast hour 22 is the result of moisture being removed and mixed into the PBL. This process continues as the convective PBL builds up and mixes out the additional moisture present in NC from the previous evening. Differences in the wind speed profile between NC and CTRL are found to be reversed from the night before, which is attributed to the additional available momentum from the previous night being mixed down to the surface for NC. A little unexpected is the substantial increase in TKE after the morning transition is complete. This is the result of an 'imbalance' between buoyancy production and dissipation in Fig. 2b, with buoyancy maintaining larger values during the day compared to dissipation. One might expect more of an impact on the mean structure by added turbulence, which is not evident in this case. The lack of impact on the mean structure is also noted in the small differences in PBL height between CTRL and NC included in Fig. 4 (green v. gray lines). This is not surprising, however, since the PBL height is diagnosed by the bulk Richardson Number in equation A3, which depends both on the the mean wind and temperature structure, both of which do not change appreciably.

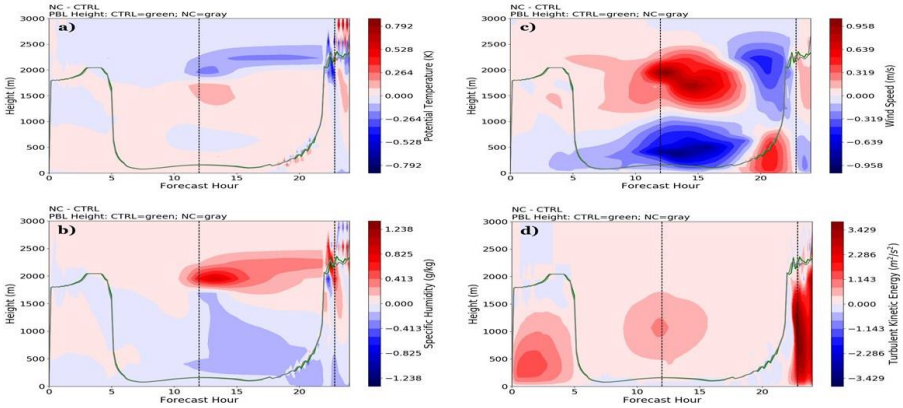

Figure 4: Time-height cross-section of the difference between No Constraint and CTRL (NC – CTRL) for a) potential temperature, b) specific humidity, c) wind speed, and TKE. Overlaid is PBL height for CTRL (green) and NC (gray). The vertical dashed lines represent specific times used for profile analysis in the discussion section. The original cross-section from the CTRL run is represented by Fig. 1.

b. Sensitivity of Stratification by Wind Shear on Mixing Length

Following Rodier et. al. (2017), we apply an adjustment to the asymptotic mixing length by including a wind shear term shown in equation (7). The Rodier et. al (2017) study determined a tuning coefficient of 0.5 based on calibration efforts while the next version of the sa-TKE-EDMF scheme plans to adopt a coefficient of 0.2. Our experiment is comprised of five cases with the shear coefficient set to 0, 0.25, 0.5, 0.75, and 1. Setting the coefficient to zero reproduces the results from CTRL.

Figure 5 shows the vertically integrated terms of the TKE equation from equation A2 applied across the PBL for shear coefficients of 0.25, 0.5, 0.75, and 1.0. The control case where the shear coefficient was set to zero is identical to the plot in Fig. 2a. In each case the basic features are the same: buoyancy is largely balanced by dissipation during the day, and what little shear production there is in the evening is destroyed by negative buoyancy and dissipation. Focusing first on the transition toward a convective PBL into the afternoon, it clear that the amount of buoyancy generated varies, but is almost exactly balanced by dissipation regardless of what the tuning parameter is set to. Moreover, it is difficult to determine the exact impact of increasing the shear coefficient since the differences do not necessarily lead to proportional changes in the turbulent and mean structure, at least at first glance. What changes there are to TKE with time coincide with transport as evidenced by the overlapping behavior of the green and black lines in Fig. 5.

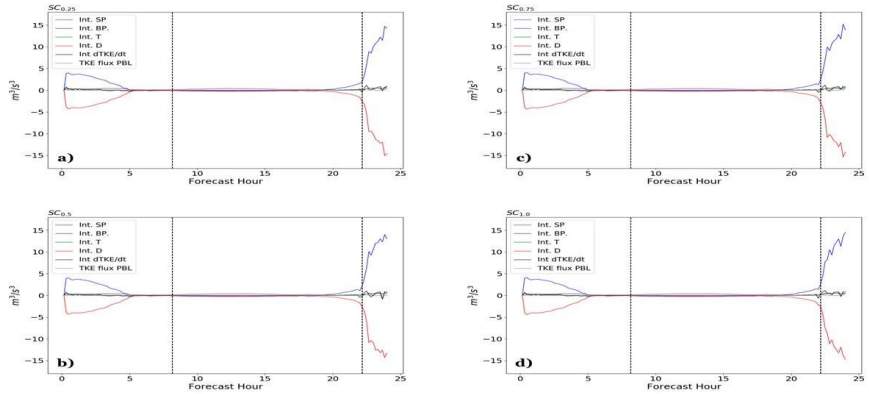

Figure 5: Vertically integrated TKE budget for shear coefficients from equation 7 set a) 0.25, b) 0.5, c) 0.75, and d) 1.0. The vertical dashed lines encompass the window for analysis of stable PBL and residual layer. Reference case is found in Fig. 2a.

Since the behavior in the stable PBL is dwarfed by daytime behavior, we include zoom-in plots confined by the dashed lines in Fig. 5 of both the turbulence within the PBL (below LLJ height maximum) and within the residual layer (above LLJ height maximum) for shear coefficients of 0.5 and 1.0 in Figure 6. Interestingly, the bulk energetics is virtually indistinguishable within the stable PBL between all cases. The effect of increasing the tuning parameter is to effectively limit the depth that a parcel will travel by considering the impact of dynamic stratification by wind shear (Rodier et al. 2017). By comparing the dissipation between Fig. 3a and Fig. 6a-b, it is clear that altering the tuning coefficient had little effect. An explanation that comes to mind is that despite the large amount of wind shear produced in the PBL from the LLJ, the eddy viscosity itself is very small, and so the amount of wind shear responsible for generating TKE is not significant enough for a parcel to move non-locally. The maximum amount of TKE within the PBL for all cases falls 0.77 $m^2\ s^{-2}$ and 0.81 $m^2\ s^{-2}$, thus giving further credence to this supposition by the fact that the right hand side of equation (7) is small and because the thermodynamic/dynamic stratification is large enough to suppress turbulence from mixing over the depth of the PBL.

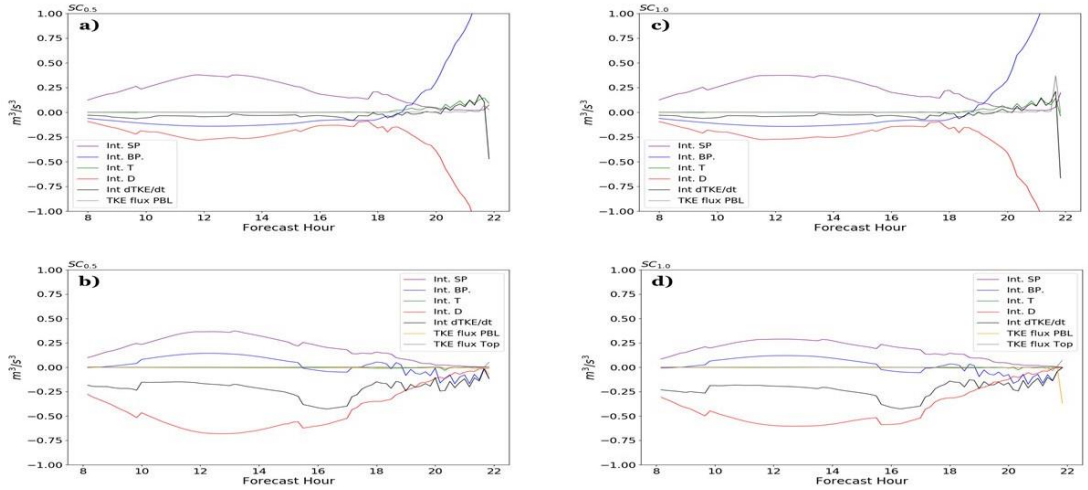

Figure 6: The vertically integrated TKE budget for a) c_0=0.5 - stable PBL, b) c_0=1 - stable PBL, c) c_0=0.5 – Residual layer, and d) c_0=1 – Residual layer. Reference plots for comparison are found in Fig. 3a-b.

Unlike the stable PBL, the residual layer shows considerable more variability between cases. Similar in magnitude to the terms within the PBL, the combined production by wind shear and buoyancy is exceeded by dissipation, thus resulting in a decrease in the bulk layer TKE w.r.t. time as shown in Fig. 6c-d for a shear coefficient of 0.5 and 1.0, respectively – a result similar to that shown in Fig. 2b for CTRL. The enhanced production above the LLJ maximum in Fig. 6c-d is linked to a more sheared profile and buoyancy, perhaps due to dynamic lift into a relatively un-stratified layer or by an accelerating LLJ. Interestingly, increasing the wind shear coefficient leads to a decrease in all terms, and in particular the shear production and dissipation. During the morning transition, the results generally show shear production and dissipation converging to zero while further decreases in TKE are matched by negative buoyancy as the stratified under-layer of the stable PBL begins to ascend during convection initiation.

Differences with CTRL are presented in Figure 7a-d for wind speed and TKE, with results from setting the shear coefficient to 0.5 and 1.0 shown in Fig. 7a-b and Fig. 7c-d, respectively. We chose not to show potential temperature or moisture since differences were negligible in most places outside the upper regions of the convective PBL, and were at most a difference of 1K and 1 g/kg, respectively. Departures in the wind speed profile, however, show a more meaningful relationship that can be easily linked to the application of the tuning coefficient. Increasing it from

0 to 1, for instance, increases not only the strength of the LLJ but the wind shear accompanying it. Although the largest differences are at most 1-m/s, it shows the sensitivity of adjusting this coefficient and its anticipated impact. Moreover, the increase in shear along with a stronger LLJ also coincides with higher dissipation and a relative decrease in the vertically integrated TKE tendency (Fig. 5) and TKE (Fig. 6) despite there being an increase in production at the same time (Fig. 6a-d). As night transitions to day, a reverse occurs in the wind profile such that winds near the surface decrease while simultaneously increasing aloft by a similar magnitude seen during the evening. This 'polarity switch' in the profile between night and day follows a similar explanation as in the previous section; namely, that there is more momentum available from the previous night's LLJ when increasing the shear coefficient, which is then transported towards the surface as the convective boundary layer grows and interacts with the layers aloft. As in the previous section, the PBL heights for all cases shown in Fig. 7 do not change appreciably owed to the fact that the mean structure varies little when adjusting the shear coefficient. There is some indication, however, that increasing the shear coefficient has some impact on timing in that the PBL climaxes slightly earlier than CTRL.

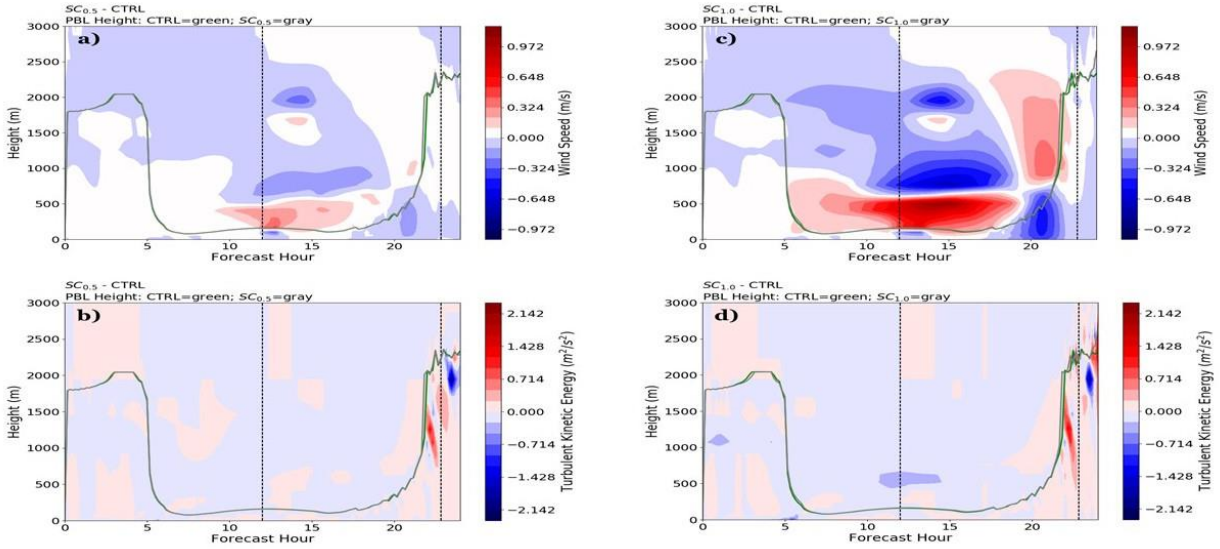

Figure 7: Time-height cross-sections of the difference between for a) c_0=0.5 and CTRL – Wind speed, b) c_0=0.5 and CTRL – TKE, c) c_0=1 and CTRL – Wind speed, and d) c_0=1 and CTRL – TKE. PBL heights are overlaid for CTRL (green) and experiment (gray). The vertical dashed lines represent specific times used for profile analysis in the discussion section. The original cross-section from the CTRL run is represented by Fig. 1.

c. MYNN Mixing Lengths

Replacing the current mixing lengths with formulations found in the MYNN scheme (MLS) results in a significant difference between the balance of terms that make up the TKE budget, particularly during the day. Figure 8 shows more dissipation relative to buoyancy, which results in a persistent decrease of the vertically integrated TKE tendency despite larger buoyancy production. In all other cases except NC, the buoyancy was largely balanced out by dissipation, with the variability of the integrated TKE tendency following closely with TKE transport. This 'imbalance' between buoyancy and dissipation is related to the direct substitution of the original length scales with MLS. Another peculiarity is the strong dips in buoyancy which also coincide with dips in dissipation. These differences are related to intermittent decreases in TKE not present in CTRL or the other experiments. Compared to CTRL, the magnitude of the integrated buoyancy and dissipation is larger when running with MLS. The MLS experiment replaces the BouLac formulation with equation (10), and applies different tuning coefficients to the surface layer length scales given in column 3 of table 1. Moreover, a turbulent length scale was added, with a blending approach that adopts equation 12 rather than equation 11.

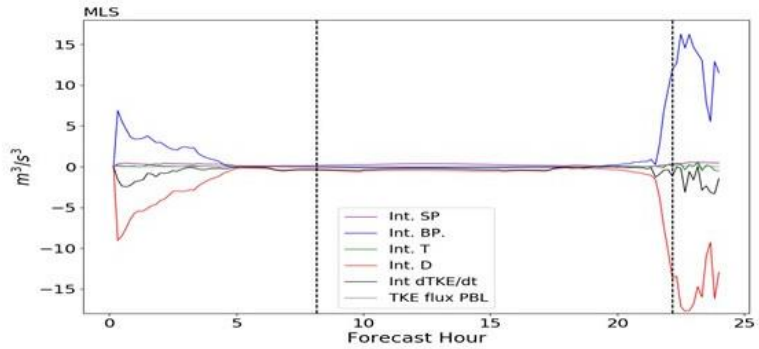

Figure 8: Vertically integrated TKE using MYNN length scales (MLS). Reference case is found in Fig. 2a. The vertical dashed lines encompass the window for analysis of stable PBL and residual layer.

Figures 9a-b show the integrated TKE budget for the stable PBL and residual layer, which can be compared with CTRL in Fig. 3a-b. Remarkably, there are almost no differences between buoyancy and shear production prior to the morning transition. The impact on dissipation, however, is clear, with integrated values twice as large when using MLS. This leads to larger negative tendencies as a result and thus a reduction in turbulence via TKE balance. By forecast hour 18, the differences between other terms for CTRL and MLS becomes evident. For CTRL, the buoyancy and dissipation are almost exactly balanced, with the integrated TKE tendency increasing along with transport as night transitions to day. Similar to findings from Fig. 3a, the dissipation when using MLS is larger than buoyancy, thus contributing to a more negative TKE tendency. Comparisons between CTRL and MLS in the residual layer, on the other hand, reveal differences between all terms. Although the magnitude of dissipation is consistently larger when using MLS, the decrease in the integrated TKE tendency is somewhat offset by increases in both shear and buoyancy production. Differences during the night-to-day transition between CTRL and MLS is minimal since shear production and dissipation tend toward zero while negative buoyancy between cases is of a similar magnitude, thereby resulting in a similar evolution of the integrated TKE tendency.

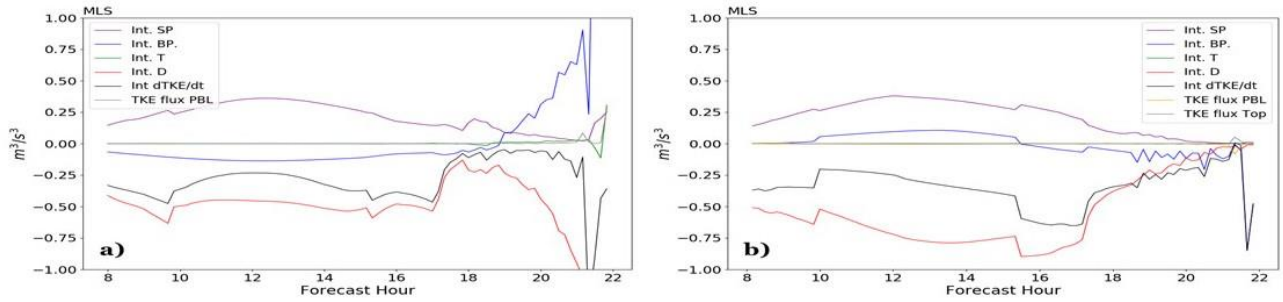

Figure 9: Vertically integrated TKE budget for a) stable PBL and b) residual layer using MYNN length scales (MLS). Reference plots for comparison are found in Fig. 3a-b.

Comparing the mean structure between CTRL and MLS helps to address some of the differences in the bulk energetics as a function of time. Aside from the small increase in temperature during the evening across both the stable PBL and residual layer in Fig. 10a - likely the cause of an increased moisture layer in Fig.10b overlying the residual layer and supported by relatively cooler longwave radiation heating rates (not shown) – is the stronger super-adiabatic layer when applying MLS following the morning transition at forecast hour 21. This, evidently, results not only in stronger transport of heat and moisture (differences as large as 5K and 3 g/kg in Fig. 10a and

Fig. 10b, respectively), but more aggressive PBL growth as shown by the differences in PBL heights overlaid in Fig. 10. This can be understood by considering the Bulk Richardson Number in equation A3; namely the PBL is larger when using MLS since the thermal gradient is more super-adiabatic and more negatively sloped across a larger depth (refer to differences in Fig. 10a-b), thus resulting in larger negative values that gradually cross-over to the critical Richardson Number at a higher height than CTRL. This also leads to larger buoyancy across the depth of the PBL as shown in Fig. 8 and reveals the vast majority of the buoyancy increase occurs in the upper half of the convective PBL as the PBL reaches maximum height. As in the other cases, the dissipation naturally matches these patterns, but with the dissipation consistently larger than buoyancy production. This impacts the amount of TKE generated, which counterintuitively leads to a decrease in TKE despite the PBL height being higher.

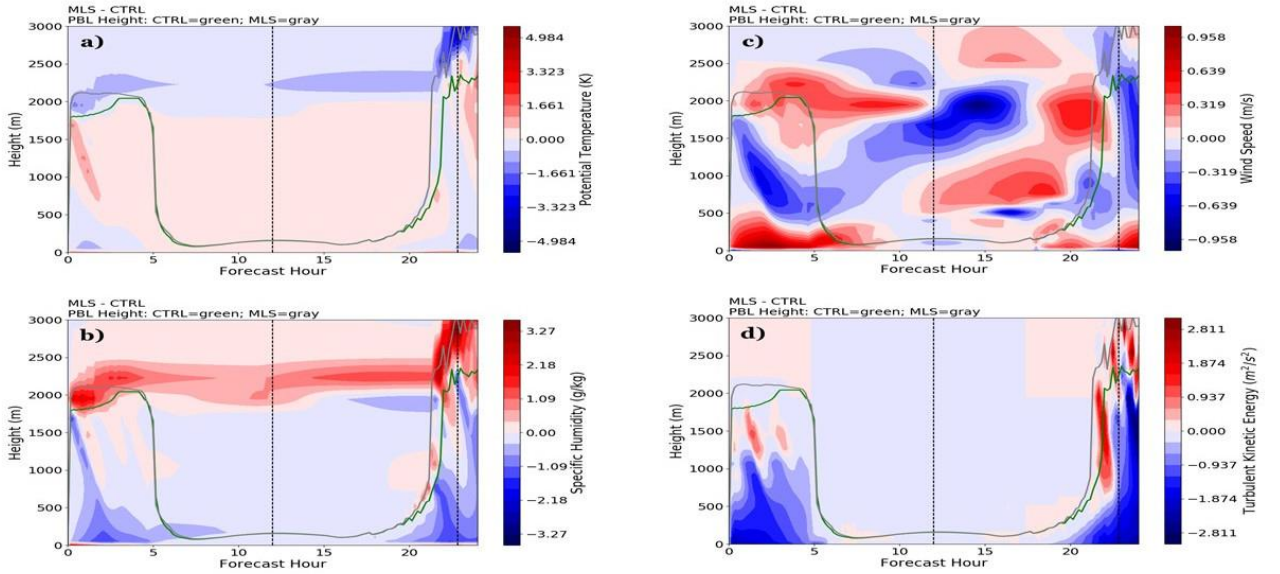

Figure 10: Time-height cross-section of the difference between MLS and CTRL for a) potential temperature, b) specific humidity, c) wind speed, and d) TKE. Overlaid is PBL height for CTRL (green) and MLS (gray). The vertical dashed lines represent specific times used for profile analysis in the discussion section. The original cross-section from the CTRL run is represented by Fig. 1.

As mentioned earlier, MLS exhibits strong intermittent variations of turbulent and mean fields during the day while all other configurations exhibit more gradual behavior. The differences in Figs. 10a-b, d that appear negatively slanted suggests a removal of moist mass at the top of the PBL that extend across the column toward the surface. This is shown by the subsequent decrease/increase in heat/moisture along axis of the slant, followed by a decrease of moisture once it is removed. The combined behavior, either through cause and effect or simultaneously, is believed to be the cause for the substantial variability when applying MLS.

Impacts of applying the MLS in the evening are evident by examining the differences in the wind profile and dissipation w.r.t. time. The LLJ that sets up in the evening has smaller acceleration rates based the temporal variation of differences between CTRL and MLS in Fig. 10c. Moreover, during the evening, the wind profile across the LLJ appears smaller below 500-m by forecast hour 10, with slightly stronger winds above that extend in excess of 1000-m for the remainder of the evening. The decrease in winds coincides with increased dissipation; but since differences in TKE across this layer appear negligible, then it must be related to having smaller mixing lengths across a thin layer of the PBL near the surface in the MLS configuration.

5. Discussion

In the previous section we examined the sensitivities of using different tuning parameters on the mixing length scales as well as the application of a different mixing length formulation on the bulk energetics and the mean structure. In this section we examine the evolution of shear and buoyancy production terms near the surface, and take a closer look at the turbulent and mean structure during individual times delineated by vertical dashed lines shown in the time-height cross-sections. The specific times chosen for profile analysis are forecast hours 12 and 22.83 since they represent a maximization in LLJ strength and TKE production for the former, and a fully developed convective PBL for the latter.

a. Assessing Turbulent Structure During Peak Winds

Figure 11 shows the vertical profiles of wind speed (Fig. 11a-c), TKE (Fig. 11d-f), and the blended mixing length (Fig. 11h-i), or master length scale, for forecast hour 12. Overlaid on each of the plots are observations from the tower (black squares) and sounding data where relevant (gray line).

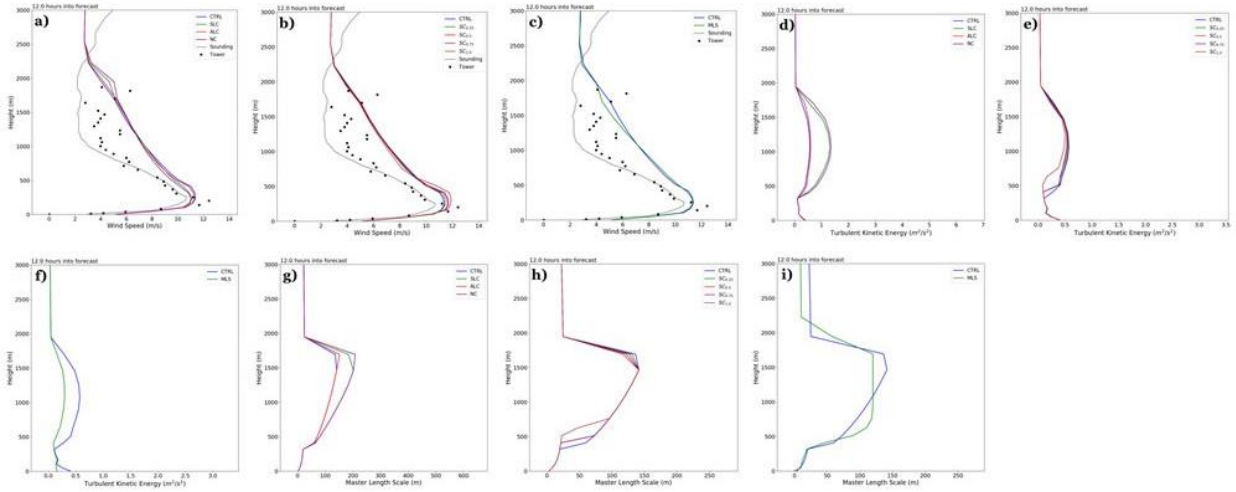

Figure 11: Profiles of wind speed (a-c) for experiment testing a) mixing length constraints, b) different shear coefficients, c) MYNN length scales; middle row from left to right is TKE for d) Mixing length constraints, e) different shear coefficients, f) MYNN length scales; bottom row from left to right (g-i) is blended length scales for g) Mixing length constraints, h) different shear coefficients, i) MYNN length scales. Over laid on the top top row is wind speed observations from the tower (black squares) and sounding (gray line). The time of analysis is forecast hour 12.

The upper panel (Fig. 11a-c) reveals small variations in wind speed near the LLJ maximum and near the top of the residual layer. It is clear when comparing the different constraints in Fig. 11a that the asymptotic mixing length (i.e. constraint only on surface layer length scale, SLC) has more of an impact than just releasing the constraint on the surface layer length scale (ALC) since the behavior of the former follows closer to NC than the other two; and, furthermore, produces a less sheared profile (i.e. green and purple lines). This agrees with Fig. 11d, which shows a more turbulent residual layer for NC and SLC. Interestingly, the substantially larger amounts of turbulence produced does little in the way of significantly reducing the sheared profile despite turbulence being enhanced. This is likely because the blended length scale used in the dissipation calculation is twice as large across the residual layer (Fig. 11g), which is enough to offset the impact of increased TKE in the dissipation calculation as shown earlier in Fig. 3b-c. Also of note is the identical profile structure within the stable PBL in Fig. 11 regardless of whether the constraints are applied or not, which is mainly owed to the fact that length scales within the stable boundary physically don't reach the 300-m capping limit. In terms of agreement with

observations, the simulations all produce an LLJ comparable in magnitude to both the tower and radiosonde, but fail to capture both the shear structure in the residual layer; and tend to agree more with each other than observations regardless of the experiment tested. This demonstrates the innate challenges of reproducing a profile structure resembling observations.

Modifying the tuning coefficient, and therefore the impacts of wind stratification on the profile structure, is shown by an increasingly stronger LLJ (Fig. 11b), a less turbulent profile (Fig. 11e), and a decrease in the blended length scale at levels near the LLJ maximum and at the top of the residual layer (Fig. 11h). The impacts within the stable PBL are again, minimal, while changes between experiments appear rooted in the residual layer. Although increasing the shear coefficient produces an increasingly energetic LLJ, the changes to TKE and the blended length scale are minimal except when the shear coefficient is set to 1. In fact, setting the shear coefficient to 1 results in a negative shear profile that is similarly sloped to observations while the other cases are more distributed in the vertical. Since there was quite an increase in the integrated dissipation from Fig. 6d, then it stands to reason that the substantial decrease in the mixing length in the lower part of the residual layer is the cause.

The impact of replacing the current mixing length formulation with MYNN length scales is evident across both the stable PBL and residual layer. Although differences in the wind speed profile are nearly negligible in Fig. 11c, the differences in the turbulent structure (Fig. 11f) and blended length scale (Fig. 11i) are apparent. Supplanting the mixing length formulation results in a reduction in TKE across the lower half of the PBL and across the entire residual layer. Moreover, the blended length scale exhibits a different vertical structure than the original formulation by placing more emphasis on larger length scales near the base of the residual layer. This change in behavior on the mixing length may be undesirable, however, because if TKE remains unchanged between cases – hypothetically – then less dissipation would be applied above the LLJ maximum, thereby potentially leading to a more diffuse wind profile structure. Nevertheless, there are some positive impacts on the upper portion of the wind profile near the residual layer top since the master length scale remains smaller, and thus results in a more sheared profile sloped closer to observations as a result of the increased dissipation.

Since profiles of the TKE budget were found to be less informative during the evening for this case – mainly owed to the broadly feature structure across the residual layer as well as negligible to minute variations within the PBL – we chose, instead, to examine the time evolution of buoyancy production/destruction and shear production near the surface. Moreover, because the departures from CTRL were found to be largest in NC, MLS, and when the shear coefficient was set to 1, only an examination of these cases are presented. Figs. 12a-b shows the buoyancy production/destruction term at 60-m and 100-m, respectively. During the evening, the buoyancy destruction term is nearly identical between all cases, with a noted increase in magnitude as the evening progresses. Compared to observations, the buoyancy destruction appears too large, and likely contributes to an over-suppression of turbulence. Of more interest is the shear production at 60-m and 100-m shown in Figs. 12c-d. Both CTRL and when the shear coefficient is set to 1 produces larger shear production compared to NC and MLS. NC in particular, shows a consistent reduction compared to all cases. Interestingly, adjusting the shear coefficient to 1 results in a local increase in shear production around forecast hour 15 that is augmented at 100-m compared to the other configurations. This seems to line up with what is seen in observations at that time despite observations exhibiting much smaller shear production values. Another point worth mentioning is the rather broad peak and distribution that encompasses the strengthening/weakening time period of the LLJ. This is quite different than what is seen in observations, which shows a narrower peak that occurs earlier than what is predicted.

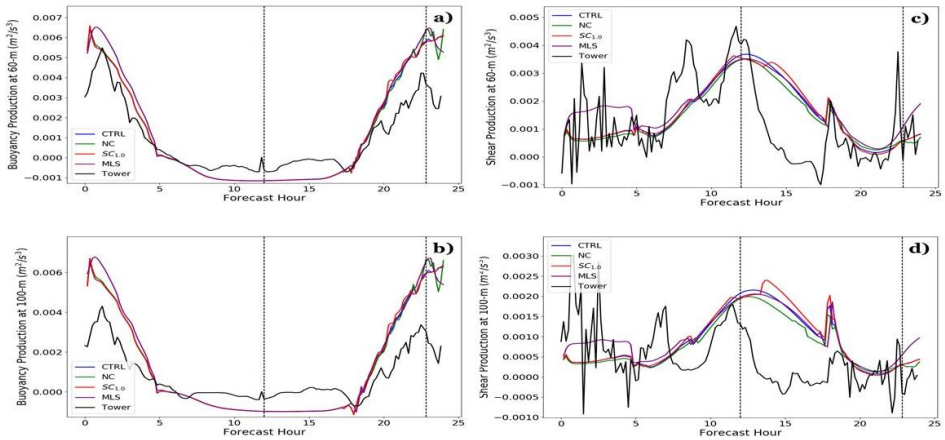

Figure 12: Time series of a) buoyancy production/destruction at 60-m, b) buoyancy production/destruction at 100-m, c) shear production at 60-m, and d) shear production at 100-m. Overlaid is observations from the Tower as shown by the black line. The vertical dashed lines represent specific times used for profile analysis in the discussion section.

b. Structure of the Convective PBL

The profiles shown at forecast 22.83 are for potential temperature (Fig. 13a-c), TKE (Fig. 13d-f), and the blended length scale (Fig. 13g-i). Apart from the experiment conducted to examine MLS, the potential temperature for all remaining experiments varies little in the structure except with some small differences near PBL top. The potential temperature comparison in Fig. 13c, however, is of interest given the substantial impact that was found on the PBL height and the turbulent structure below. Consistent with Fig. 10a, a more super-adiabatic layer is produced with the MLS configuration. Both exhibit a near neutral profile up to 1500-m before the behavior begins to diverge significantly aloft, with the inversion setting up at a higher height in MLS. Compared to available observations, most simulations are able to produce a similar structure, albeit warmer. The only experiment that is somewhat of an outlier is MLS, which shows a structure that is too super-adiabatic.

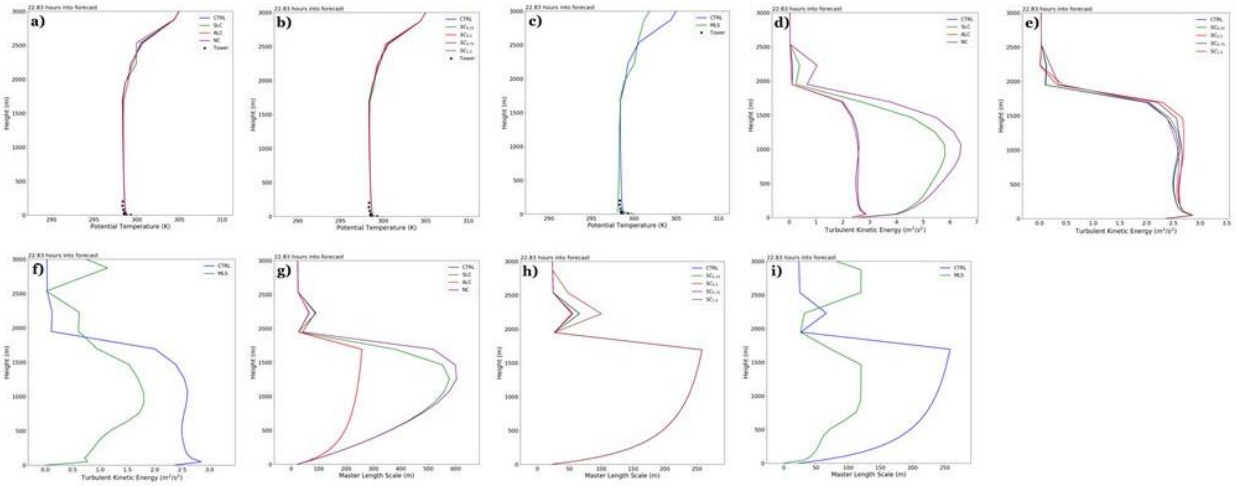

Figure 13: Profiles of potential temperature (a-c) for experiment testing a) mixing length constraints, b) different shear coefficients, c) MYNN length scales; middle row from left to right is TKE for d) Mixing length constraints, e) different shear coefficients, f) MYNN length scales; bottom row from left to right (g-i) is blended length scales for g) Mixing length constraints, h) different shear coefficients, i) MYNN length scales. Over laid on the top row is wind speed observations from the tower (black squares) and sounding (gray line). The time of analysis is forecast hour 22.83.

The TKE profiles shown when constraints are placed on the mixing lengths (Fig. 13d) are wildly different during convective conditions. Based on similar arguments made earlier, it is clear that the asymptotic mixing length formulation is the main source of this departure given that dissipation depends on its calculation. The relative increase in the blended length scale in Fig. 13g appears substantial enough to offset the increase in TKE based on equation 4. This leads to the imbalance shown in Fig. 2b, which is also corroborated in Fig 14.

Differences in TKE when changing the shear coefficient are rather small for convective conditions and vary unpredictably based on the TKE profiles in Fig. 13e. The master length scale shows no detectable differences below 2000-m in Fig. 13h. However, above that height, there is a substantial increase in the mixing length scale for c0=1 and a decrease when c0=0.75. Although this is just a snapshot, it does appear that changes are most impactful near PBL top while having a minimal impact near the surface.

The amount of TKE generated at forecast hour 22.83 for MLS compared to CTRL (Fig. 13f) matches the behavior found in the master length scale (Fig. 13i). Substantially lower length scale values at this time leads to larger dissipation if the denominator in equation 4 decreases more sharply than any increase of TKE in the numerator. This is reversed above 2000-m as the CTRL case shows a simultaneous increase/decrease in TKE/length scale compared the experimental run, which explains the differences in TKE found in Fig. 10d. It should be noted that the MLS configuration produced much more variable conditions in the daytime as described in the Results section. It should also be mentioned that the buoyancy/turbulent length scales carried over from the MYNN are dependent on TKE as well as dissipation itself. This results in a hyper dependence of TKE in the dissipation calculation which may prove problematic in certain situations. Another likely explanation is that sa-TKE-EDMF is not tuned to handle the MYNN formulations. Although these formulations work well for the MYNN scheme, it is clear that they produce undesirable results in the sa-TKE-EDMF scheme.

The budget profiles for TKE in Figure 14 (same experiments as in Fig. 12) all exhibit similar behavior, with dissipation largely being balanced by buoyancy production, and the TKE tendency following along TKE transport. Differences from CTRL (Fig. 14a) mainly occur with the magnitude of dissipation/buoyancy (Fig. 14d), the vertical extent of the buoyancy/dissipation and transport (all cases vary with one another), and an increase in buoyancy destruction near the base of the inversion (Fig. 14d). The decrease in transport near the surface is related to TKE being transported aloft to higher levels as indicated by an increase in transport across the mid-to-upper portion of the PBL (all cases). The degree to which transport varies can't be gleaned from examining one profile alone; however, the magnitude of transport is reduced in MLS (Fig. 14d) and increased significantly in NC (Fig. 14b).

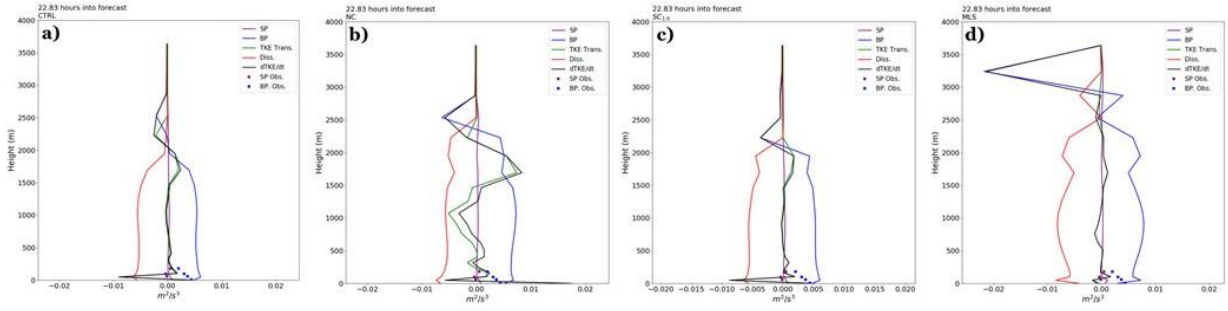

Figure 14: from top and left to right is the TKE budget for a) CTRL, b) No constraint, c) when the shear coefficient is set to 1, and d) using MYNN length scales. Overlaid is observations from the Tower of shear production (purple squares) and buoyancy destruction (blue squares). Time of analysis is forecast hour 22.83.

What's clear is that the imbalance noted in MLS appears related to an enhanced buoyancy destruction terms at the base of the inversion. This marked decrease is a likely source of the decreased integrated buoyancy term relative to the integrated dissipation shown in Fig. 8. In each case the buoyancy that is generated is considerably larger at lower levels compared to observations. This is in line with results from Fig. 12a-b, which show an overabundance of buoyancy for all configurations compared to observations. The NC and MLS configurations depart more from CTRL, with relatively larger buoyancy early (intersecting the profile analysis time) followed by a decrease shortly after. Shear production from the model output during the day is of less interest; however, compared to observations in Fig. 12c-d, it is evident that the intermittency of turbulence via shear production from observations is not being produced, even partially, for any of the configurations tested in this study.

6. Conclusion

In this paper we evaluated a series of experiments by testing the sensitivity of either tuning specific coefficients or replacing the current mixing length scale formulation altogether. The goal was not to find out a preferred configuration, but rather understand the sensitivity of using different tuning parameters and mixing length formulations. A technique was introduced to examine the bulk energetics in both the PBL and residual layer, which helped to understand how the TKE balance approach in sa-TKE-EDMF changed over time. Our findings from this study revealed the following:

- Most experiments except NC and MLS show a balance between buoyancy and dissipation during the day with the TKE tendency following TKE transport. During the evening, a clear decrease in the bulk TKE tendency in the stable PBL is evident, with the buoyancy destruction and dissipation outweighing shear production. The degree to which this balance changes is subtle except in the case of the experiment running with MYNN mixing length formulations. For that experiment the TKE tendency decreased relative to other experiments as a result of large decreases in buoyancy near the base of the inversion and a relative increase in integrated dissipation compared to buoyancy. This was a result of smaller mixing lengths in the PBL and lower residual layer that led to larger negative TKE tendencies.
- Releasing of constraints on the original mixing length resulted in situations where both the surface layer length scale and asymptotic length scale exceeded the 300-m cap by 400-m to 700-m, the former unrealistically so. While both length scales increased markedly, it was found that releasing the asymptotic mixing length constraint had far more of an impact on increased TKE, which is corroborated by the fact that the bulk representation of buoyancy within the convective PBL exceeded dissipation. This can be understood by the fact that only the BouLac formulation is being applied to the dissipation length scale (equation 11b); and since an increase in the dissipation length scales occur when releasing the constraint, the overall dissipation, too, must decrease. It is interesting to note that the mean structure changes very little despite the 'imbalance' that results when releasing the asymptotic mixing length constraint.
- Testing of different shear coefficients in the modified BouLac form of equation 7 was most impactful within the residual layer. Regardless of what the shear coefficient was set to, both the mean structure and the bulk energetics remained the same. Increasing the shear coefficient, and in particular for coefficients in excess of 0.5, resulted in a clear increase in both buoyancy and shear production as the winds of the LLJ increased in magnitude (about 1 m/s). This, however, was largely balanced by increased dissipation owed to a decrease in the mixing lengths in the lower/upper halves of the residual layer. The mean structure of the LLJ was clearly impacted as evidenced by increasing LLJ wind speeds with increasing shear coefficient. The larger coefficients resulted in a shear profile that

was more sloped to observations. Differences in the daytime were likely the result of more momentum being mixed down as stronger winds from the night before contained more momentum overall with increasing shear coefficients, and therefore the potential to mix down more momentum.

- Replacing the current mixing formulations with MYNN formulae resulted in substantial departures from the CTRL case, both in terms of bulk energetics and the mean structure. While buoyancy and shear terms in the TKE equation changed to a minimal degree both within the stable PBL and residual layer, the dissipation was greatly increased owed to overall decreases in both the surface layer length scales and turbulent/buoyancy length scales. This resulted in quite a decrease in the bulk TKE tendency for both layers when using MYNN formulae. Interestingly, however, was the lack of impact on the LLJ structure with time except in the upper portion of the residual layer. Differences in both the bulk energetics and mean structure during the daytime was found to be much larger. As in the case when releasing the asymptotic mixing length constraint, an imbalance between dissipation and buoyancy occurred within the PBL. However, this imbalance was a result of larger integrated dissipation relative to integrated buoyancy, which thereby reduced the bulk TKE tendency. The imbalance was in part attributed to very large negative values of buoyancy at PBL top, while all other terms remained small or converged to zero. The mean structure was also impacted to a greater degree, particularly for potential temperature and moisture. The experiment running with MYNN length scales yielded a much stronger super adiabatic layer, which significantly modified the both the turbulent structure and representation of buoyancy. Moreover, the intermittent behavior present in this experiment – but not so much the others – appeared related to the increased moisture above the residual layer and the occasional mixing down toward the surface during the morning transition. Owed to stronger super-adiabatic conditions, this was the only case that showed a significant increase in PBL height relative to CTRL.
- Lastly, the representation of shear and buoyancy production was found to be significantly different compared to observations at low-levels. All configurations were too negatively (positively) buoyant during the night (day) compared to observations. Shear production was also too broadly distributed and failed to exhibit any intermittent behavior indicated by observations.

Based on the results presented, we believe that the logical next step is to find other ways to target the different boundary layer types. Since the stable PBL was insensitive to the experiments conducted except when using MYNN formulae, then other changes, either to the stability functions or the production/destruction terms themselves, would be of significant importance. Stable PBLs are often plagued with runaway cold biases owed to a lack of mixing. Some studies have pointed to including gravity waves/shear waves in the momentum mixing process (Finnigan 1999; Sun et. al. 2015). Other studies have found that using total turbulent energy closure leads to better representations of stable PBLs if the variance in potential temperature is prognosed (Zilitinkevich et. al. 2007). It also appears important that a balance is struck between dissipation and buoyancy production during convective conditions. If an imbalance occurs, this seems to greatly impact the mean structure in a way that's undesirable. More analyses would need to be conducted to separate the role of ED v. MF in the sa-TKE-EDMF scheme to better determine this affect.

Appendix A

a. Bulk Characterization of TKE

In order to characterize the bulk characteristics of TKE as it relates to production, dissipation, and transport, we examine the time rate of change of the integrated behavior bounded by two surfaces. The two surfaces in question can either represent the stable PBL as the lower limit and the top of the residual layer as the upper limit, or the surface as the lower limit and PBL as the upper limit. We make use of the Leibnez integration rule to put the time rate of change of the vertically integrated TKE into a more usable form using equation A1.

$$\frac{d}{dt}\int_{z_{pbl}(t)}^{z_R(t)} \bar{e}\,dz = w_R(t)\bar{e}(z_R(t),t) - w_{pbl}(t)\bar{e}\big(z_{pbl}(t),t\big) + \int_{z_{pbl}(t)}^{z_R(t)} \frac{\partial \bar{e}(z,t)}{\partial t} dz \qquad \text{(A1)}$$

Here, $w_R(t) = \frac{dz_R(t)}{dt}$ and $w_{pbl}(t) = \frac{dz_{pbl}(t)}{dt}$ is the change in residual layer and PBL height w.r.t. time. The integral of the TKE tendency on the R.H.S. of equation A1 can be rewritten in terms of the TKE budget.

$$\int_{z_{pbl}(t)}^{z_t(t)} \frac{\partial \bar{e}}{\partial t} dz = \int_{z_{pbl}(t)}^{z_R(t)} \frac{g}{\bar{\theta}_v} \overline{w'\theta_v'} dz - \int_{z_{pbl}(t)}^{z_R(t)} \left(\overline{w'u'}\frac{\partial U}{\partial z} + \overline{w'v'}\frac{\partial V}{\partial z} \right) dz - \int_{z_{pbl}(t)}^{z_R(t)} \frac{\partial \overline{w'e'}}{\partial z} dz - \int_{z_{pbl}(t)}^{z_R(t)} \varepsilon dz \qquad \text{(A2)}$$

The expression in equation A2, plus the flux terms of mean TKE across the bounded surfaces, is used for the above analysis when examining the residual layer, but with the integral expression replaced with parameterized forms of the fluxes. If we instead chose the lower bound as the surface and the upper bound as PBL height, then the second term in A2 would disappear while $w_R(t)$ becomes $w_{PBL}(t)$. All terms are plotted with negligible contributions found for the mean fluxes across the bounded surfaces and integrated TKE transport in most situations. Although these terms are negligible for the model output in this analysis, it is suspected that these terms may have an appreciable contribution for certain real world situations, and may prove meaningful when using a high spatiotemporal resolution instrument like a Doppler LIDAR. Changes in entrainment and the morning transition are situations where these terms are likely to have a more substantial contribution, both of which are situations where numerical models struggle.

b. Algorithmic Approach for Isolating the Residual Layer

In order to successfully determine the upper-bound – in this case the residual layer – we first need to determine the height closest to PBL top. From there, an interpolation of TKE to the exact height of the PBL can be done followed by a vertical iteration scheme up to the height of the residual layer. The iteration scheme relies on the Bulk Richardson number in equation A3 and its gradient.

$$Ri_b = \frac{\frac{g\Delta\theta}{\theta\Delta z}}{\left(\frac{\Delta U}{\Delta z}\right)^2 + \left(\frac{\Delta V}{\Delta z}\right)^2} \qquad \text{(A3)}$$

Since the height of the PBL is determined by the critical Richardson number, and the profile above the stable boundary tends toward neutral in the residual layer, we begin first with the condition of examining whether the bulk Richardson number becomes negative (i.e. the thermal gradient reverses). If we iterate through to model top, then we break the loop and instead look at the vertical gradient of the Bulk Richardson number; otherwise if a negative Richardson Number is

determined then we search for the next instance that the critical Richardson Number is reached. The vertical gradient of Richardson Number is also used based on the fact that stratification decreases away from the stable PBL (refer to Fig. A1). The first condition is represented symbolically by equation (A4), while the second set conditions is represented by A5.

$$z_0 = \sum_{z_{PBL}<z<z_{top},\ Ri<0} Ri_b(n) \tag{A4}$$

$$z_R = \begin{cases} \sum_{z_n<z_{PBL}, \frac{\partial Ri_b(n)}{\partial z}<0} \frac{\partial Ri_b(n)}{\partial z}, & z_0 == z_{top} \\ \sum_{Ri<Ri_c} Ri_b(n), & z_0 < z_{top};\ \frac{\partial Ri_b(n)}{\partial z} > 0 \end{cases} \tag{A5}$$

The second condition in A5 is applied if z_0 did not reach model top or if the first condition in A5 is met. These conditions are the basis for identifying the residual layer since a stratified layer will ultimately be reached again once we transition from the residual layer to the free atmosphere. Figure A2 shows an example where heights of both the PBL and residual layer top have been determined with potential temperature overlaid.

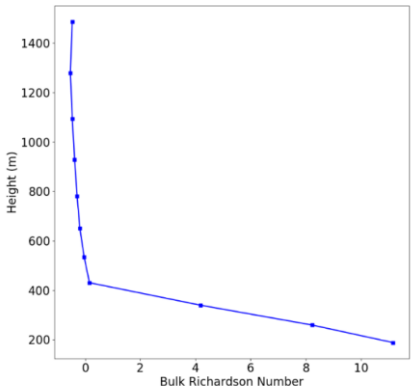

Figure A1: Plot of bulk Richardson number above stable PBL. Notice it decreases to nearly zero before inflecting toward higher values near residual layer top.

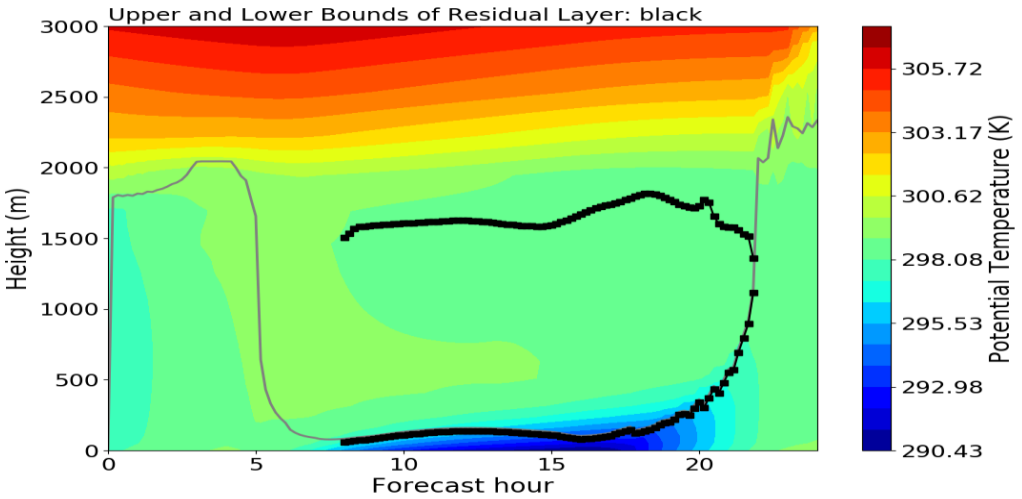

Figure A2: Potential temperature overlaid with PBL height (gray) as well as the upper and lower bounds of the residual layer (black squares).

References

1. Abdella, K. and McFarlane, N., 1997. A new second-order turbulence closure scheme for the planetary boundary layer. *Journal of the atmospheric sciences*, *54*(14), pp.1850-1867.
2. Aligo, E.A., Ferrier, B. and Carley, J.R., 2018. Modified NAM microphysics for forecasts of deep convective storms. *Monthly Weather Review*, *146*(12), pp.4115-4153.
3. Baklanov, A.A., Grisogono, B., Bornstein, R., Mahrt, L., Zilitinkevich, S.S., Taylor, P., Larsen, S.E., Rotach, M.W. and Fernando, H.J.S., 2011. The nature, theory, and modeling of atmospheric planetary boundary layers. *Bulletin of the American Meteorological Society*, *92*(2), pp.123-128.
4. Blackadar, A.K., 1962. The vertical distribution of wind and turbulent exchange in a neutral atmosphere. *Journal of Geophysical Research*, *67*(8), pp.3095-3102.
5. Bosveld, F.C., Baas, P., van Meijgaard, E., de Bruijn, E.I., Steeneveld, G.J. and Holtslag, A.A., 2014. The third GABLS intercomparison case for evaluation studies of boundary-layer models. Part A: Case selection and set-up. *Boundary-layer meteorology*, *152*(2), pp.133-156.
6. Bougeault, P. and Lacarrere, P., 1989. Parameterization of orography-induced turbulence in a mesobeta--scale model. *Monthly weather review*, *117*(8), pp.1872-1890.
7. Chakraborty, A., 2010. The skill of ECMWF medium-range forecasts during the year of tropical convection 2008. *Monthly weather review*, *138*(10), pp.3787-3805.
8. Cuo, L., Pagano, T.C. and Wang, Q.J., 2011. A review of quantitative precipitation forecasts and their use in short-to medium-range streamflow forecasting. *Journal of hydrometeorology*, *12*(5), pp.713-728.
9. Duan, Q., Schaake, J., Andreassian, V., Franks, S., Goteti, G., Gupta, H.V., Gusev, Y.M., Habets, F., Hall, A., Hay, L. and Hogue, T., 2006. Model Parameter Estimation Experiment (MOPEX): An overview of science strategy and major results from the second and third workshops. *Journal of Hydrology*, *320*(1-2), pp.3-17.
10. Finnigan, J., 1999. A note on wave-turbulence interaction and the possibility of scaling the very stable boundary layer. *Boundary-Layer Meteorology*, *90*(3), pp.529-539.
11. Grell, G.A. and Freitas, S.R., 2014. A scale and aerosol aware stochastic convective parameterization for weather and air quality modeling. *Atmos. Chem. Phys*, *14*(10), pp.5233-5250.
12. Grossman, S.A., 1996. A theory of non-local mixing-length convection-III. Comparing theory and numerical experiment. *Monthly Notices of the Royal Astronomical Society*, *279*(2), pp.305-336.
13. Han, J., Wang, W., Kwon, Y.C., Hong, S.Y., Tallapragada, V. and Yang, F., 2017. Updates in the NCEP GFS cumulus convection schemes with scale and aerosol awareness. *Weather and Forecasting*, *32*(5), pp.2005-2017.
14. Han, J. and Bretherton, C.S., 2019. TKE-based moist Eddy-Diffusivity Mass-Flux (EDMF) parameterization for vertical turbulent mixing. *Weather and Forecasting*, *34*(4), pp.869-886.
15. Janić, Z.I., 2001. Nonsingular implementation of the Mellor-Yamada level 2.5 scheme in the NCEP Meso model.
16. Lamberson, W.S., Torn, R.D., Bosart, L.F. and Magnusson, L., 2016. Diagnosis of the source and evolution of medium-range forecast errors for extratropical cyclone Joachim. *Weather and Forecasting*, *31*(4), pp.1197-1214.
17. Lenderink, G. and Holtslag, A.A., 2004. An updated length-scale formulation for turbulent mixing in clear and cloudy boundary layers. *Quarterly Journal of the Royal*

Meteorological Society: A journal of the atmospheric sciences, applied meteorology and physical oceanography, *130*(604), pp.3405-3427.
18. Lin, Y.L., Farley, R.D. and Orville, H.D., 1983. Bulk parameterization of the snow field in a cloud model. *Journal of Applied Meteorology and climatology*, *22*(6), pp.1065-1092.
19. Lock, A.P., Brown, A.R., Bush, M.R., Martin, G.M. and Smith, R.N.B., 2000. A new boundary layer mixing scheme. Part I: Scheme description and single-column model tests. *Monthly weather review*, *128*(9), pp.3187-3199.
20. McTaggart-Cowan, R., Vaillancourt, P.A., Zadra, A., Chamberland, S., Charron, M., Corvec, S., Milbrandt, J.A., Paquin-Ricard, D., Patoine, A., Roch, M. and Separovic, L., 2019. Modernization of atmospheric physics parameterization in Canadian NWP. *Journal of Advances in Modeling Earth Systems*, *11*(11), pp.3593-3635.
21. Mellor, G.L. and Yamada, T., 1974. A hierarchy of turbulence closure models for planetary boundary layers. *Journal of the atmospheric sciences*, *31*(7), pp.1791-1806.
22. Mellor, G.L. and Yamada, T., 1982. Development of a turbulence closure model for geophysical fluid problems. *Reviews of Geophysics*, *20*(4), pp.851-875.
23. Mishra, A.A. and Girimaji, S.S., 2017. Toward approximating non-local dynamics in single-point pressure–strain correlation closures. *Journal of Fluid Mechanics*, *811*, pp.168-188.
24. Morrison, H. and Gettelman, A., 2008. A new two-moment bulk stratiform cloud microphysics scheme in the Community Atmosphere Model, version 3 (CAM3). Part I: Description and numerical tests. *Journal of Climate*, *21*(15), pp.3642-3659.
25. Muñoz-Esparza, D., Sauer, J.A., Linn, R.R. and Kosović, B., 2016. Limitations of one-dimensional mesoscale PBL parameterizations in reproducing mountain-wave flows. *Journal of the Atmospheric Sciences*, *73*(7), pp.2603-2614.
26. Nakanish, M., 2001. Improvement of the Mellor–Yamada turbulence closure model based on large-eddy simulation data. *Boundary-layer meteorology*, *99*(3), pp.349-378.
27. Nakanishi, M. and Niino, H., 2004. An improved Mellor–Yamada level-3 model with condensation physics: Its design and verification. *Boundary-layer meteorology*, *112*(1), pp.1-31.
28. Nakanishi, M. and Niino, H., 2009. Development of an improved turbulence closure model for the atmospheric boundary layer. *Journal of the Meteorological Society of Japan. Ser. II*, *87*(5), pp.895-912.
29. Noh, Y., Cheon, W.G., Hong, S.Y. and Raasch, S., 2003. Improvement of the K-profile model for the planetary boundary layer based on large eddy simulation data. *Boundary-layer meteorology*, *107*(2), pp.401-427.
30. Olson, J.B., Kenyon, J.S., Angevine, W., Brown, J.M., Pagowski, M. and Sušelj, K., 2019. A description of the MYNN-EDMF scheme and the coupling to other components in WRF–ARW.
31. Pleim, J.E., 2007. A combined local and nonlocal closure model for the atmospheric boundary layer. Part I: Model description and testing. *Journal of Applied Meteorology and Climatology*, *46*(9), pp.1383-1395.
32. Randall, D.A. and Pan, D.M., 1993. Implementation of the Arakawa-Schubert cumulus parameterization with a prognostic closure. In *The representation of cumulus convection in numerical models* (pp. 137-144). American Meteorological Society, Boston, MA.
33. Rodier, B., de Leon, A., Hemmingsen, C. and Pentzer, E., 2017. Controlling oil-in-oil pickering-type emulsions using 2D materials as surfactant. *ACS Macro Letters*, *6*(11), pp.1201-1206.
34. Siebesma, A.P., Soares, P.M. and Teixeira, J., 2007. A combined eddy-diffusivity mass-flux approach for the convective boundary layer. *Journal of the atmospheric sciences*, *64*(4), pp.1230-1248.

35. Sun, J., 2011. Vertical variations of mixing lengths under neutral and stable conditions during CASES-99. *Journal of applied meteorology and climatology*, *50*(10), pp.2030-2041.
36. Sun, J., Nappo, C.J., Mahrt, L., Belušić, D., Grisogono, B., Stauffer, D.R., Pulido, M., Staquet, C., Jiang, Q., Pouquet, A. and Yagüe, C., 2015. Review of wave-turbulence interactions in the stable atmospheric boundary layer. *Reviews of geophysics*, *53*(3), pp.956-993.
37. Teixeira, J. and Cheinet, S., 2004. A simple mixing length formulation for the eddy-diffusivity parameterization of dry convection. *Boundary-layer meteorology*, *110*(3), pp.435-453.
38. Thompson, G., Field, P.R., Rasmussen, R.M. and Hall, W.D., 2008. Explicit forecasts of winter precipitation using an improved bulk microphysics scheme. Part II: Implementation of a new snow parameterization. *Monthly Weather Review*, *136*(12), pp.5095-5115.
39. Tian, Y. and Kuang, Z., 2016. Dependence of entrainment in shallow cumulus convection on vertical velocity and distance to cloud edge. *Geophysical Research Letters*, *43*(8), pp.4056-4065.
40. Troen, I.B. and Mahrt, L., 1986. A simple model of the atmospheric boundary layer; sensitivity to surface evaporation. *Boundary-Layer Meteorology*, *37*(1-2), pp.129-148.
41. Voudouri, A., Khain, P., Carmona, I., Bellprat, O., Grazzini, F., Avgoustoglou, E., Bettems, J.M. and Kaufmann, P., 2017. Objective calibration of numerical weather prediction models. *Atmospheric Research*, *190*, pp.128-140.
42. Zhang, H., Pu, Z. and Zhang, X., 2013. Examination of errors in near-surface temperature and wind from WRF numerical simulations in regions of complex terrain. *Weather and Forecasting*, *28*(3), pp.893-914.
43. Zilitinkevich, S.S., Elperin, T., Kleeorin, N. and Rogachevskii, I., 2007. Energy-and flux-budget (EFB) turbulence closure model for stably stratified flows. Part I: steady-state, homogeneous regimes. In *Atmospheric Boundary Layers* (pp. 11-35). Springer, New York, NY.